

Cathode Materials

Zitierweise: *Angew. Chem. Int. Ed.* **2020**, 59, 22092–22099

Internationale Ausgabe: doi.org/10.1002/anie.202008144

Deutsche Ausgabe: doi.org/10.1002/ange.202008144

Direct Observation of Defect-Aided Structural Evolution in a Nickel-Rich Layered Cathode

Shuang Li⁺, Zhenpeng Yao⁺, Jianming Zheng⁺, Maosen Fu, Jiajie Cen, Sooyeon Hwang, Huile Jin, Alexander Orlov, Lin Gu, Shun Wang,* Zhongwei Chen* und Dong Su*

Abstract: Ni-rich $\text{LiNi}_{1-x-y}\text{Mn}_x\text{Co}_y\text{O}_2$ (NMC) layered compounds are the dominant cathode for lithium ion batteries. The role of crystallographic defects on structure evolution and performance degradation during electrochemical cycling is not yet fully understood. Here, we investigated the structural evolution of a Ni-rich NMC cathode in a solid-state cell by in situ transmission electron microscopy. Antiphase boundary (APB) and twin boundary (TB) separating layered phases played an important role on phase change. Upon Li depletion, the APB extended across the layered structure, while Li/transition metal (TM) ion mixing in the layered phases was detected to induce the rock-salt phase formation along the coherent TB. According to DFT calculations, Li/TM mixing and phase transition were aided by the low diffusion barriers of TM ions at planar defects. This work reveals the dynamical scenario of secondary phase evolution, helping unveil the origin of performance fading in Ni-rich NMC.

Introduction

Rechargeable lithium ion batteries (LIBs) have been widely deployed in portable electronics devices and are gradually penetrating the market of transportation systems, such as electric vehicles (EVs), owing to their energy density dominance over traditional energy storage apparatuses.^[1] Next-

generation LIBs of higher energy density are urgently needed, which is intrinsically limited by the electrode materials upon (de)accommodating lithium ions capacity, especially the cathode side.^[2] To replace currently commercialized cathodes of LiCoO_2 and $\text{LiNi}_{1/3}\text{Mn}_{1/3}\text{Co}_{1/3}\text{O}_2$ (NMC333), nickel-rich $\text{LiNi}_{1-x-y}\text{Mn}_x\text{Co}_y\text{O}_2$ (Ni-rich NMC) layered compounds have attracted significant attentions for their sizable specific discharge capacity and superb cost effectiveness.^[3] However, Ni-rich NMC cathode presently suffers rapid performance degradations upon cycles (capacity fading and power loss).^[4] This degradation has been attributed to the structural changes initiated from the particle surface, such as the breakdown of cathode electrolyte interphase layer,^[5] surface structural reconstruction,^[4c,6] surface corrosion,^[5d,7] transition metal (TM) ion dissolution,^[5c,8] as well as the bulk structural changes, including $\text{Li}^+/\text{Ni}^{2+}$ ion exchange,^[9] phases transition^[10] and intergranular/intragranular cracks.^[10c,11] Those changes significantly reduce the reversible capacity owing to the blocked Li^+ diffusion path, induced anisotropic stress, and increased charge transfer resistance.^[3e,6a,9a,12] Previous reports on the performance-structure correlation in Ni-rich and regular NMC cathodes are summarized in the Supporting Information, Tables S1 and S2. However, these reports have not considered the effects from the crystallographic defects. It is well known that the crystallographic defects, such as dislo-

[*] Dr. S. Li,^[†] Prof. H. Jin, Prof. S. Wang
Key Laboratory of Carbon Materials of Zhejiang Province, Institute of New Materials and Industrial Technologies, Wenzhou University
Wenzhou, Zhejiang, 325027 (China)
E-Mail: shunwang@wzu.edu.cn
Dr. S. Li,^[†] Prof. Z. Chen
Department of Chemical Engineering, University of Waterloo
Waterloo, Ontario, N2L 3G1 (Canada)
E-Mail: zhwchen@uwaterloo.ca
Dr. S. Li,^[†] Dr. S. Hwang, Prof. D. Su
Center for Functional Nanomaterials
Brookhaven National Laboratory
Upton, NY 11973 (USA)
E-Mail: dongsu@iphy.ac.cn
Dr. Z. Yao^[†]
Department of Chemistry and Chemical Biology, Harvard University
12 Oxford Street, Cambridge, MA 02138 (USA),
and
Department of Chemistry and Department of Computer Science,
University of Toronto
Toronto, Ontario M5S 3H6 (Canada)

Prof. J. Zheng^[†]
Energy and Environment Directorate
Pacific Northwest National Laboratory
902 Battelle Boulevard, Richland, WA 99352 (USA),
and
College of Chemistry and Chemical Engineering, Xiamen University
Xiamen, Fujian 361005 (China)
Dr. M. Fu
State Key Laboratory of Solidification Processing, School of Materials
Science and Engineering, Northwestern Polytechnical University
Xian, 710072 (China)
Dr. J. Cen, Prof. A. Orlov
Department of Materials Science and Chemical Engineering
Stony Brook University
Stony Brook, NY 11794 (USA)
Prof. L. Gu, Prof. D. Su
National Laboratory for Condensed Matter Physics
Institute of Physics, Chinese Academy of Sciences
Beijing, 100190 (China)

[†] These authors contributed equally to this work.

 Supporting information and the ORCID identification number(s) for the author(s) of this article can be found under:
 <https://doi.org/10.1002/anie.202008144>.

cations, stacking faults, antiphase boundaries, and twin boundaries, commonly exist in lithium metal oxide electrodes.^[11a,13] Up to now, the roles of these defects on the performance decay remains elusive.

The structural defects can only be observed with transmission electron microscopy (TEM) and the technical challenge is building a proper in situ TEM cell containing liquid electrolyte. Furthermore, the local chemical inhomogeneity, secondary phases, and stress generated during delithiation can affect the structural stability and increase the mobility of defects.^[13d,14] That demands a high spatial resolution observation from the same sample region and then one can distinguish local atomic structure changes. To the best of our knowledge, how these defects affecting local structural changes during the extraction of Li^+ remains unclear, and also it is not well established how the defects and secondary phases link to the material performance degradation.

In this work, we investigated the dynamical coupling of secondary phases and structural defects in Ni-rich NMC upon delithiation using in situ biasing transmission electron microscopy (TEM) on a cross-sectional solid-state cell. We identified the co-existence of three different phases in the as-synthesized particles, that is, layered, spinel, and rock-salt, as well as the phase boundaries between them. Under biasing voltage, we observed the elongation of the antiphase bound-

ary (APB), the phase transition near the coherent twin boundary (TB), and the formation of disordered rock-salt phase induced by the Li^+ extraction inside the particle. Density function theory (DFT) calculations confirmed the thermodynamic tendency of APB formation upon delithiation. We also found that the rock-salt phase appeared at the TB was due to the kinetically more facile Li/TM exchanges at TB compared to normal crystalline order area. Therefore, these phase changes were inclined to form close to planar defects either inside particle or in surface regions, suggesting critical role of defects on the degradation of electrode. Our results provide the dynamical scenario of defects and secondary phases during delithiation, which help to unveil the origin of performance fading in Ni-rich NMC.

Results and Discussion

We built a solid-state battery inside TEM with a Nano-factory biasing TEM holder, as shown in Figure 1 a, to realize the in situ observation of the local structural changes during delithiation. As one of the representative Ni-rich NMCs, $\text{LiNi}_{0.76}\text{Mn}_{0.14}\text{Co}_{0.10}\text{O}_2$ (NMC76) has been used as cathode, showing secondary particle with a primary particle size of about 200 nm. A layer of $\text{Li}_{0.5}\text{La}_{0.5}\text{TiO}_3$ (LLTO) solid electrolyte was

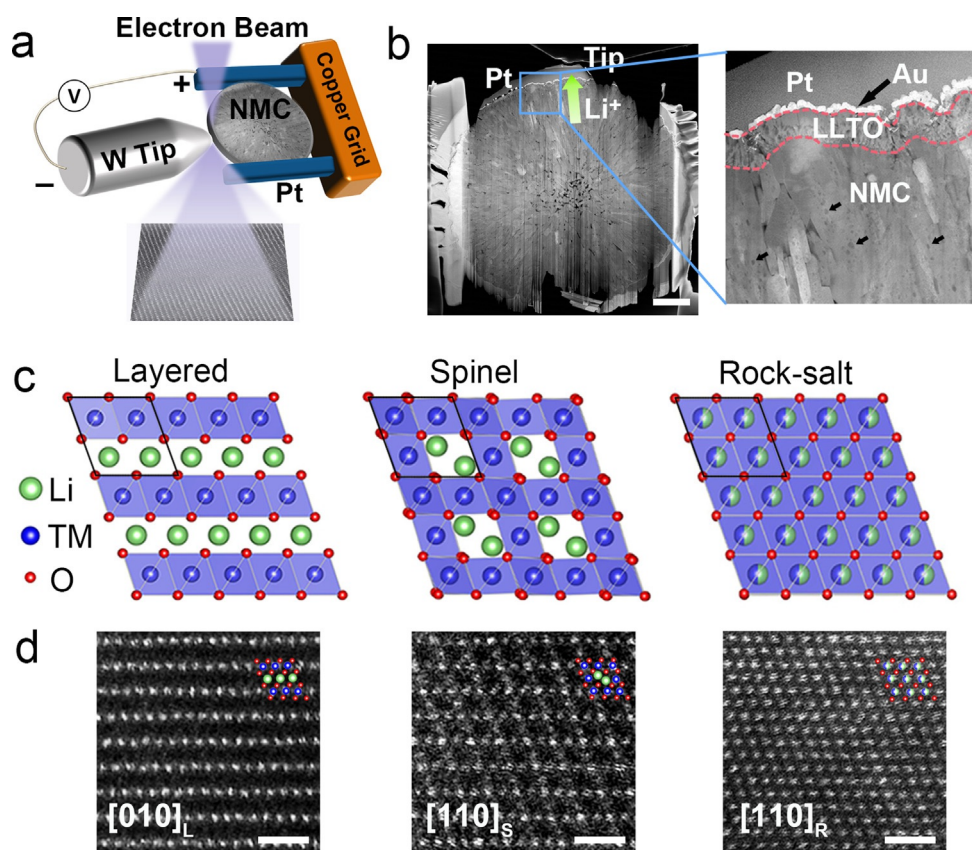


Figure 1. In situ TEM setup and the atomic structure of the phases in NMC76. a) Illustration of the in situ TEM experimental setup. b) Corresponding low magnification HAADF-STEM images showing the components of top electrode, LLTO solid electrolyte, and NMC76. The green arrow indicates the approximate direction of lithium extraction. c), d) The atomic structural models (c) and corresponding high resolution HAADF-STEM images (d) of the layered, spinel and rock-salt phases, respectively. The black rhomboids indicate the similar unit cells with cubic close packed oxygen arrays. The subscript: L: layered, S: spinel, R: rock-salt.

deposited on the surface of the NMC76 cathode by pulsed laser deposition (PLD) to provide the lithium ion extraction path and then NMC76 secondary particle was cut and polished by a focused ion beam (FIB). The prepared specimen is shown in a low magnification high angle annular dark-field scanning TEM (HAADF-STEM) image as Figure 1b. The processes of the deposition and FIB milling are detailed in the Supporting Information, Figure S1. The Au and Pt layers deposited on the sample during FIB preparation serve as the top electrode for biasing. A negative bias was applied between the tip and sample which generated an electric field to extract lithium ion out of sample as indicated by the green arrow. The elemental distributions of the NMC76 sample was obtained with a STEM-energy dispersive X-ray spectroscopy (EDX) mapping shown in the Supporting Information, Figure S2, where we can easily distinguish the NMC76 particle as well as LLTO, Au, and Pt layers.

The pristine NMC76 sample has a layered structure ($R\bar{3}m$) as indicated in X-ray diffraction (XRD) pattern (Supporting Information, Figure S3), but we found here our sample contains minor spinel and rock-salt phases which can be due to the inhomogeneous chemical composition and Li/Ni cation mixing. Layered, spinel, and rock-salt phases have similar TM-O frameworks with close lattice spacings making them coherent inside grains. The layered phase has a hexagonal structure with a space group of $R\bar{3}m$ ($a = 2.877 \text{ \AA}$, $b = 14.228 \text{ \AA}$),^[15] where the transition metal and lithium occupy octahedral $3b$ and $3a$ sites, respectively. Whereas the spinel and rock-salt phases have the space groups of $Fd\bar{3}m$ ($a = 8.219 \text{ \AA}$)^[16] and $Fm\bar{3}m$ ($a = 4.177 \text{ \AA}$), respectively, as shown in Figure 1c. The black rhombus in each phase model indicates the similar unit cells with slightly different lattice constants (Layered: $4.98 \text{ \AA} \times 5.03 \text{ \AA} \times 5.75 \text{ \AA}$, spinel: $5.03 \text{ \AA} \times 5.03 \text{ \AA} \times 5.81 \text{ \AA}$, Rock-salt: $5.12 \text{ \AA} \times 5.12 \text{ \AA} \times 5.91 \text{ \AA}$). We note that the lattice parameters can vary along with the local chemical compositions. Furthermore, the space groups of the layered and spinel phases are subgroups of the rock-salt phase, which means traditional phase boundaries should be observed. However, from a specific zone axis, it is easy to distinguish these three phases from the high-resolution HAADF-STEM images of NMC76 sample as shown in Figure 1d, where the bright spots indicate the projection of TM columns (Z-contrast). We also found some voids (small dark areas marked by black arrows in Figure 1b) in the pristine sample, which were also reported in NMC333.^[17] We have not observed any elemental inhomogeneity around these voids with STEM-electron energy loss spectroscopy (EELS) mapping (Supporting Information, Figure S4) but we deduce these voids formed during synthesis can be possibly correlated to the Kirkendall effect.^[18] In this work, no effects from voids have been found on the evolutions of either defects or phases.

It is well known that lithium diffusion in layered compounds is along a - b plane which is strongly affected by phase boundaries. The projection lattice structures of the boundaries can be considered as the overlapping of the adjacent two phases. In Figure 2, we identified five kinds of boundaries in NMC76 with high-resolution HAADF-STEM imaging. The boundaries between these phases (layered, spinel, rock-salt) show a structural coherence and therefore orientational cor-

relations, to reduce the strain energy. Figure 2a–e shows HR-HAADF-STEM images of the boundaries and the corresponding representation showing the phase orientations. Atomic models are overlapped with the boundaries with the blue circles representing TM atom columns, and cyan circles representing TM atom columns with lower occupancies. There are two typical boundaries between one layered phase with another layered phase domain. One is APB with one translation shift vector along the c direction, as shown in Figure 2a. In this case, the TM layer of one side is continuously contacted to the Li layer of the other side. The boundary has several unit cell widths region with strong contrasting dots in either the TM or Li layer, which implies the boundary plane is not strictly perpendicular to the TM plane. Figure 2b shows another type of high symmetry coherent twin boundary (TB) between layered phases, which is similar to that reported in LiCoO_2 layered material (called $\Sigma 2$ ($\bar{1}14$)[110] grain boundary).^[13b,14a] The zone axes of the two adjacent areas are $[010]$ and $[0\bar{1}0]$ with their (003) planes tilted about 109.7° from each other, as shown in the right schematic. Observed in Figure 2b, there is a wide overlapping area with spinel structure feature, which is different to the clear and sharp boundary as reported in LiCoO_2 ,^[14a] and may be caused by the stress and the high degree of TM/Li disorder in NMC76 sample. Besides the boundaries between layered phases, the boundaries between different phases have presented characteristics of overlapping regions, as shown in Figure 2c–e. Figure 2c shows the boundary between the layered and spinel phases, which has a spinel-like feature with a slightly different contrast at the TM atom column as the index shown. Figure 2d shows the boundary between the rock-salt and spinel phases, the center octahedral $16c$ site which is normal vacant in spinel unit cell shows some bright contrast and we called it disordered spinel phase boundary. Figure 2e shows the boundary between the rock-salt and layered phases, which has a disordered layered phase feature. We noted that the disordered layered phase displayed the identical feature of the ion-mixed phase. This feature can be from either overlapping or indeed the ion-mixing. Because of the similar cubic close packed oxygen arrays of these three phases, they all have a certain orientation relationship to minimize the boundary energy, as indicated in the corresponding schematic at right of Figure 2c–e: $[010]_L//[110]_S$, $(001)_L//(1\bar{1}1)_S$ and $[110]_R//[110]_S$, $(1\bar{1}1)_R//(1\bar{1}1)_S$ and $[110]_R//[010]_L$, $(1\bar{1}0)_R//(001)_L$. The boundaries between layered compounds as planar defects have been observed previously in the bulk region of delithiated or cycled NMC cathodes,^[13c,14a,19] while the boundaries facing with other minor phase, spinel or rock-salt phase, are normally observed on particle surface.^[4b,6a] The stability of these planar defects under the extraction of lithium of NMC76 will be studied in the following sections. The boundaries of these three phases in NMC76 were analyzed in Table 1.

We compared the structural changes of identical areas with HR-STEM under biasing. Figure 3a shows a HR-HAADF-STEM image of a representative area where APB and TB between layered phases were observed in the pristine sample. These defects are thought to be origin from the materials synthesis process. Figure 3b shows the image at the

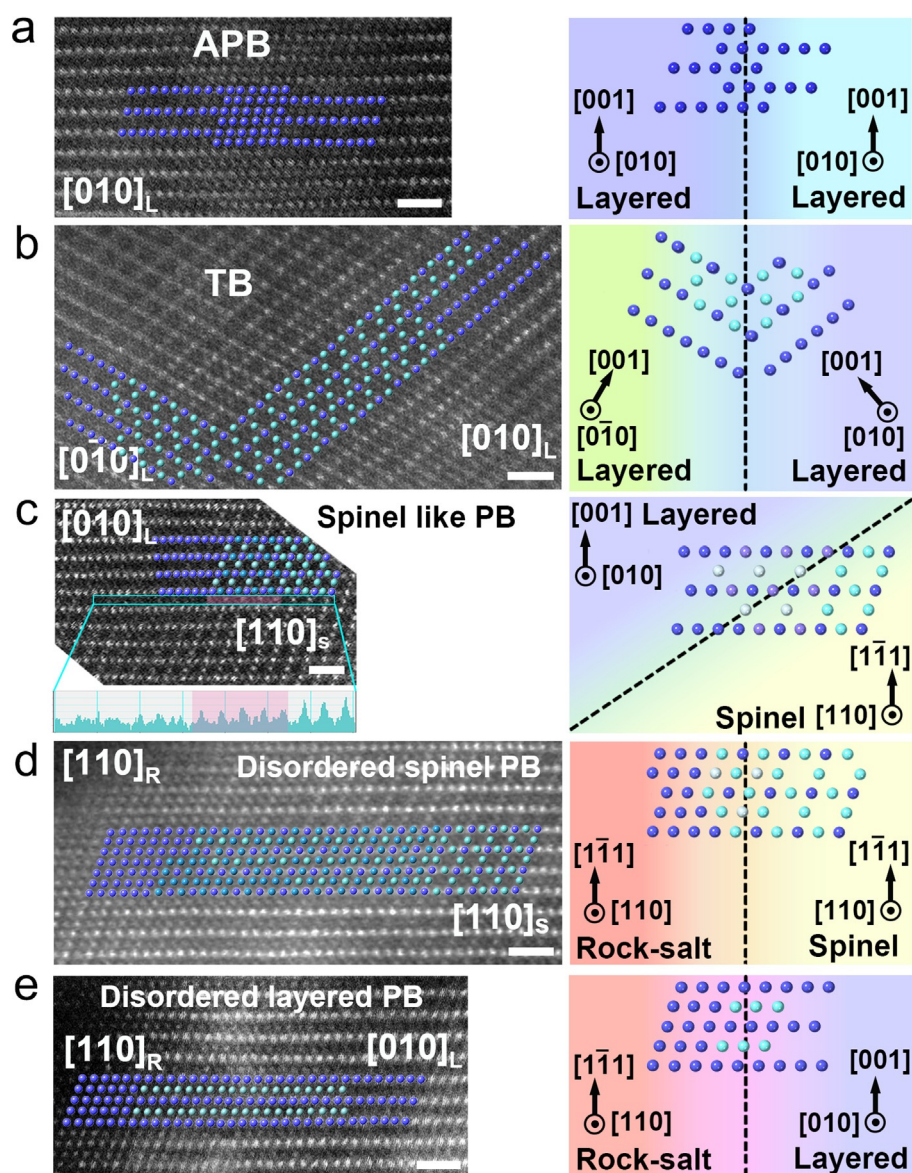


Figure 2. Atomic structure of the phase boundaries observed in NMC76. HR-HAADF-STEM images and corresponding schematic showing the phase orientations of a) APB between layered phases, b) TB between layered phases, c) spinel like phase boundary between layered phase and spinel phase, d) disordered spinel phase boundary between rock-salt phase and spinel phase near the surface region, e) disordered layered phase boundary between rock-salt phase and layered phase near the surface region. The blue spots represent TM atomic columns, cyan spots represent TM atomic columns with lower occupancies.

Tabelle 1: Boundary types between different phases.

	Layered	Spinel	Rock-salt
Layered	APB/TB	spinel-like	disordered layered
Spinel	spinel-like	spinel	disordered spinel
Rock-salt	disordered layered	disordered spinel	rock-salt

same imaging conditions from the same area after delithiation. These images were filtered using an average background subtraction filter (ABSF) method to enhance the contrast to be easily distinguished and the raw images are provided in the Supporting Information, Figure S5. Considering the images before and after delithiation in Figure 3 d, the APB here could

be clearly confirmed by the characteristic that the TM layer of one side is continuously contacted to the Li layer of the other side. The structural changes after delithiation are schematically shown in Figure 3 c, where the APB and TB are marked by magenta and blue, respectively. The extraction of lithium is supposed along (003) plane to the upright direction. For the sake of observation, the solid and dash line are used to represent the boundaries ignoring the width of boundary. The solid lines represent boundaries before biasing, while the dash lines represent boundaries after delithiation. Comparing Figure 3 a and b, there is no sign of phase transition from O3 to O1, which is consistent with prior studies.^[10c,20] Figure 3 d–f are enlarged figures of the areas marked in Figure 3 a and b, respectively. The APB in Figure 3 d extends from 4 nm to

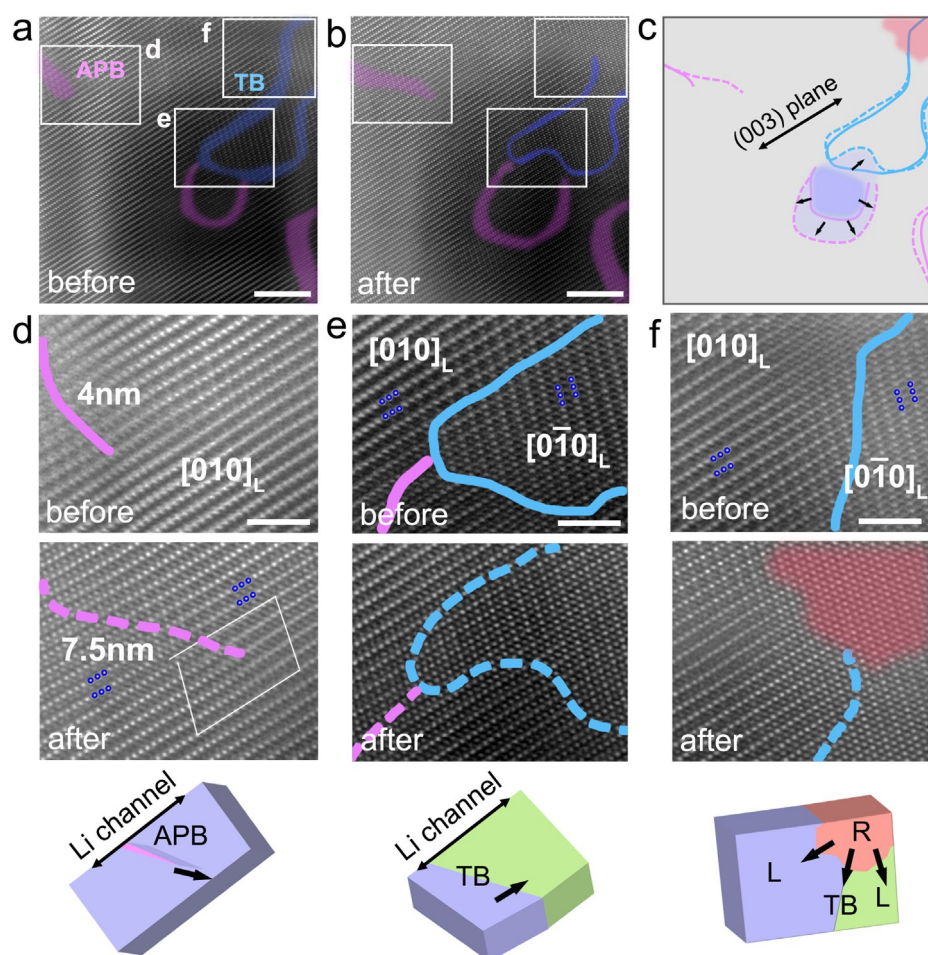


Figure 3. Interior structural changes before and after delithiation. a), b) HR-HAADF-STEM images of the same region before and after delithiation. The magenta and blue areas marked APB and TB, respectively. c) Illustration showing the phases extension and defects migration extract by comparing (a) and (b). The solid lines represent boundaries before reaction, while the dash lines represent boundaries after reaction. The red and purple areas display the layered and rock-salt phases. d)–f) The enlarged images of white rectangles in (a) and (b), and corresponding schematics. The black arrows indicate the phase extension directions and also the lithium ion diffusion channels.

7.5 nm through the movement of a partial dislocation with a Burgers vector of $1/6[211]$. From the images before and after delithiation, it is observed that the APBs moved faster along the a - b plane than crossing a - b plane, which is probably because the (003) plane containing vacancies at Li^+ sites is favorable for the movement of TM cations and dislocation. Besides APB, the TB at this area shifts a little along (003) plane, as shown in Figure 3 c and e. In Figure 3 f, cation mixing is largely enhanced along the TB at the top right area of the image, where disordered rock-salt phase appears. It is concluded from above results that with delithiation the phase transition from order to disorder is prompted, especially along the planar defects (TB).

Previous studies reported the phase evolution from layered to disordered layered or spinel, and then to rock-salt close to the surface of the layered cathode particle.^[6a,b,7,13a,21] It was believed that this TM ion migration caused surface reconstruction and blocked the lithium ion diffusion channel, leading to the large irreversible capacity.^[12a] Meanwhile, the formation of rock-salt phase usually accompanied by the oxygen loss which may induce capacity reduc-

tion, rapid voltage decay and lead to structure instability and thermal runaway.^[4d,11a,16] However, some other reports suggested that the rock-salt phase on the surface can be beneficial on the reversibility due to the pillaring effect.^[3c,7,22] Here, we also investigated the evolution of TB close to the surface region during delithiation. We chose the surface region near the LLTO layer as shown in Figure 4 a, marked by yellow arrows. From the HR-HAADF-STEM image of pristine NMC76 in Figure 4b, the TB can be easily observed, which has a broad area with a spinel phase feature (the original images are shown in the Supporting Information, Figure S6), as discussed in Figure 2 b. After delithiation, the rock-salt phase appeared at the surface and kept propagating inwardly, as shown in Figure 4c. The Figure 4d and e are the enlarged images of the marked area of Figure 4b and c, respectively, showing the atomic disordering. There is a weak contrast in the central sites of some spinel unit cells in Figure 4d, which implies there are some cation migrations in the TB at surface area before reaction. As shown in Figure 4 f, the rock-salt phase near surface also extends gradually along the TB during delithiation, which is identical to what we observed

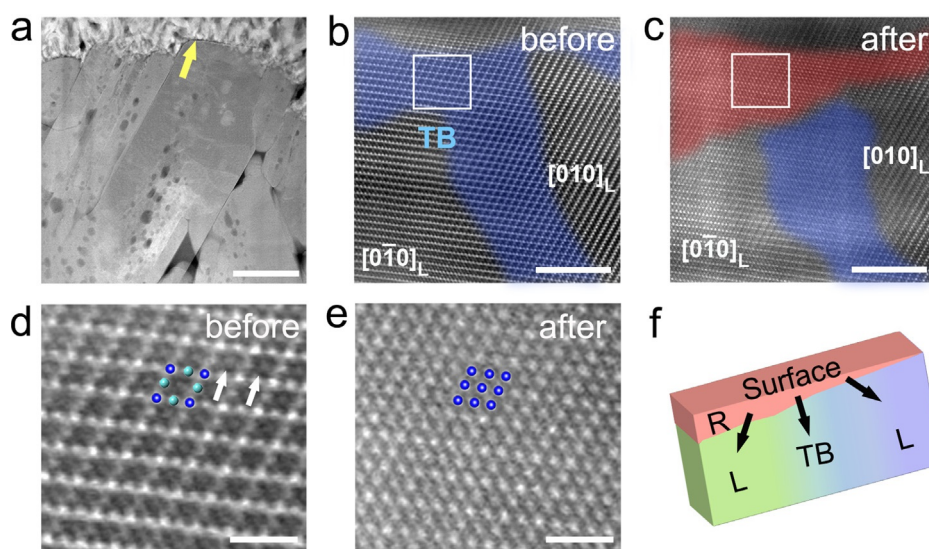


Figure 4. Structural evolution close to the surface region. a) The low magnification HAADF-STEM image of the observed primary particle. b),c) The filtered atomic scale HAADF-STEM images before (b) and after (c) delithiation of the surface region marked by yellow arrow. The blue and red areas marked TB and rock-salt phase, respectively. d),e) The enlarge images of white rectangles in (b) and (c) showing the spinel and rock-salt phases features. The white arrows indicate the weak light contrasts in the central sites of unit cells. f) The schematic illustration showing the rock-salt phase generates at the surface after delithiation.

inside NMC76 particle. In our in situ TEM experiments, we observed the biasing indeed extracted lithium ion from the structure and then induced the structural changes along planar defects, though we could not quantify the amount of extracted Li^+ .

APB was observed to extend, glide, and enlarge during the delithiation process, as shown in Figure 3. And the expansion along (003) plane seems to be faster than perpendicular directions. To understand this phenomenon, we built a structural model of the NMC76 phase with APB introduced through partially shifting the metal layers by $1/6[211]$ (Supporting Information, Figure S7). The ratio between Ni Mn:Co was settled as 9:2:1 with the simulated stoichiometry to be $\text{LiNi}_{3/4}\text{Mn}_{1/6}\text{Co}_{1/12}\text{O}_2$, approaching the experimentally determined composition. We evaluated the thermodynamic tendency on APB formation via calculating the energy difference between NMC76 configurations with and without APB in a function of Li content. As shown in Figure 5a, the energy difference between the systems with APB and without APB is a small value of 57 meV/atom as the extraction of Li is $x=0$, which indicates the possible existence of APB in as-synthesized NMC76, as we observed in Figure 2 and 3. With the extraction of Li, the energy difference increases to 110 meV/atom at $x=0.24$ and eventually approaches zero when 0.8 lithium ion per formula has been extracted. This could happen around an APB where the lattice distortion, electronic conductivity and local chemistry can facilitate Li diffusion^[13c] and prompt a Li depletion state. The calculated energy differences imply that the APB formation could occur in an early stage of delithiation at domains where the Li depletion is more likely to occur at particle surfaces, grain boundaries, and dislocations as observed in this study.^[23] The extension of APB can be attributed to gradual development of Li depletion region originated from surfaces/defects during delithiation of the particle.

Phase transformations basically proceed with the migrations of atoms inside the crystal structure, such as that the phase transition from layered structure to rock-salt is initiated with the TM diffusion to the lithium layer. Therefore, the trend of phase transition can be evaluated through computing the related energetic barriers of all ion migrations. To investigate the impact of TB on the layered \rightarrow rock-salt phase transformation in NMC76, we evaluated the kinetics of a series of reaction steps around TB in the NMC76 cathode. Meanwhile, we calculated the energetic barriers of TM ion diffusion in pristine NMC76 structure as the reference. Ni, which is the mobile TM ion in our system, was picked in this study to represent the TM atoms.^[6c] Structure models were built with TB along (104) interface (Supporting Information, Figure S9) based on the experimental observations in Figure 2c. In pristine NMC76, TM(Ni) diffusion has been proven to be rather difficult with large barriers both within the TM layer (2.11 eV) and from the TM layer to the Li layer (1.20 eV), as shown in Figure 5b, indicating the difficulty of any TM migration related phase transition in pristine NMC76. For the NMC76 with a TB, we first calculated the barrier of the vacancy assisted Li diffusion along the TB (i), as shown in Figure 5c. A small value of 0.41 eV is obtained, implying the relatively fast Li transport along the boundary during the Li extraction. Moreover, the removal of Li in the boundary creates vacancies to facilitate the following TM (Ni) migration (ii) from the TM layer to the Li layer. An anisotropic barrier (Figure 5d) is observed with a modest forward barrier of 0.68 eV implies the notable potential for the initiation of layered \rightarrow rock-salt phase transition. However, a larger backward barrier of 0.94 eV indicates the difficulty for Ni to migrate back to its original position shedding light on the irreversible layered \rightarrow rock-salt phase transition. Then we calculated the TM (Ni) diffusion barrier towards the bound-

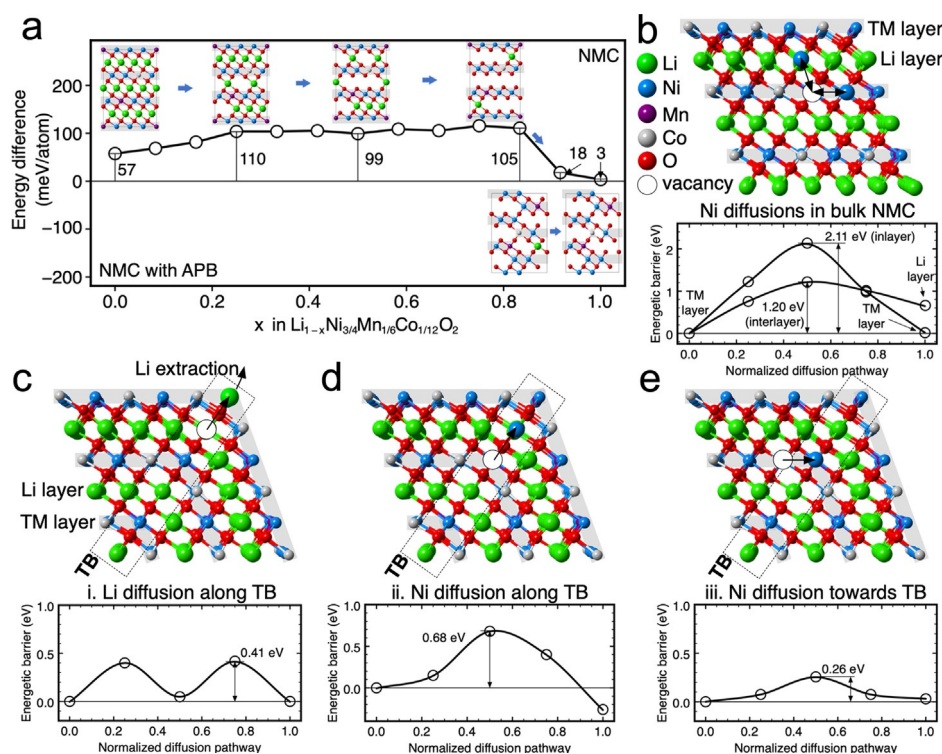


Figure 5. Calculations on the thermodynamic tendency of anti-phase boundary formation and the energetic impact of the twin boundary on the kinetics of TM ions migration in the Ni-rich NMC structure. a) The energy difference between the systems with APB and without APB. The inserts are the thermodynamically stable structure at different delithiation states. b) TM(Ni) diffusion pathways in the pristine Ni-rich NMC: in the TM layer and from TM layer to Li layer. c)–e) The kinetics of a series of reaction steps required by the layered \rightarrow rock-salt phase transformation. The Li diffusion along the TB (c), which creates vacancies to facilitate the following step TM(Ni) migration from the TM layer to the Li layer (d) to initiate the phase transition. Then, the TM(Ni) diffusion towards the boundary (e) to assist the development of the phase transition.

dary (iii), as shown in Figure 5e with a rather small barrier of 0.26 eV obtained. Afterward, many of the TM (Ni) ions will continue to make a further migration step to the Li layer as in the (ii) step. Therefore, the facile TM (Ni) migration towards TB can be seen as a sign that more and more TM ions will diffuse to the Li layer and participate in the phase transition, which will eventually lead to the growth of the rock-salt phase. As a result, the presence of TB facilitates both the initiation and development of the layered \rightarrow rock-salt phase transition, confirming the experimental observations that the rock-salt phase grows around the TB in the NMC76 particle. The experimental and consistent simulation results concurrently imply that the Li ion diffusion is strongly affected by these two defects during delithiation. In particular, the TB would facilitate the TM migration and then phase transition which could have a detrimental effect on the battery performance.

Conclusion

The structural evolution of Ni-rich NMC76 cathode during delithiation was investigated by in situ TEM. Distinguished from previous works which generally focused on the phase transitions at particle surfaces, we here confirmed for the first time the formation of Li secondary phase inside the particle aided by crystallographic defects. We classified the

boundaries between three phases (layered, spinel, rock-salt), namely APB, TB, spinel-like, disordered spinel and disordered layered, and identified them with high-resolution STEM imaging. Under in situ biasing, we found the extension of APB induced by delithiation. The formation energy of APB could be largely decreased upon deep lithium ion deintercalation as suggested by DFT calculations. On the other hand, the increasing Li/TM mixing or appearance of rock-salt phase were observed around TB after delithiation, in both surface and bulk region. Our calculations indicated TB could provide a feasible diffusion pathway for Li and TM migration with smaller energetic barriers, resulting in disordering and rock-salt phase formation. Structurally, the propagation of APB with blocked Li diffusion path may result in increased resistance for Li ion extraction and intercalation, meanwhile, the phase transition towards rock-salt phase will aggravate the electrode degradation during battery cycling. Our studies indicate that the degradation mechanisms of the Ni-rich NMC material are beyond surface determined, the inhomogeneous lithium extraction and TM migration caused by defects inside the bulk also show a significant impact. Our study can assist the development of the effective approach in suppressing secondary phase formation and design Ni-rich NMC electrodes with improved cyclability for high energy density LIBs.

Acknowledgements

This work was supported by the University of Waterloo and Wenzhou University, the National Natural Science Foundation of China (U1909213, 51772219 and 51872209). This research used resources of the Center for Functional Nanomaterials, which is a U.S. DOE office of Science Facility, at Brookhaven National Laboratory under contract No. DE-SC0012704. Computations were performed on the niagara supercomputer at the SciNet HPC Consortium. SciNet is funded by: the Canada Foundation for Innovation; the Government of Ontario; Ontario Research Fund—Research Excellence; and the University of Toronto. Dong Su acknowledges the support from the Strategic Priority Research Program (B) (grant No. XDB07030200) of Chinese Academy of Sciences.

Conflict of interest

The authors declare no conflict of interest.

Stichwörter: cathode materials · defects · in situ transmission electron microscopy · lithium ion batteries · phase transitions

- [1] a) J. M. Tarascon, M. Armand, *Nature* **2001**, *414*, 359–367; b) V. Etacheri, R. Marom, R. Elazari, G. Salitra, D. Aurbach, *Energy Environ. Sci.* **2011**, *4*, 3243; c) H. Li, *Joule* **2019**, *3*, 911–914.
- [2] a) J. B. Goodenough, Y. Kim, *Chem. Mater.* **2010**, *22*, 587–603; b) J. W. Choi, D. Aurbach, *Nat. Rev. Mater.* **2016**, *1*, 16013.
- [3] a) K. Kang, Y. S. Meng, J. Bréger, C. P. Grey, G. Ceder, *Science* **2006**, *311*, 977–980; b) H.-J. Noh, S. Youn, C. S. Yoon, Y.-K. Sun, *J. Power Sources* **2013**, *233*, 121–130; c) C. S. Yoon, M. H. Choi, B.-B. Lim, E.-J. Lee, Y.-K. Sun, *J. Electrochem. Soc.* **2015**, *162*, A2483–A2489; d) J. Li, H. Liu, J. Xia, A. R. Cameron, M. Nie, G. A. Botton, J. R. Dahn, *J. Electrochem. Soc.* **2017**, *164*, A655; e) W. Liu, P. Oh, X. Liu, M. J. Lee, W. Cho, S. Chae, Y. Kim, J. Cho, *Angew. Chem. Int. Ed.* **2015**, *54*, 4440–4457; *Angew. Chem.* **2015**, *127*, 4518–4536.
- [4] a) A. Manthiram, J. C. Knight, S.-T. Myung, S.-M. Oh, Y.-K. Sun, *Adv. Energy Mater.* **2016**, *6*, 1501010; b) Q. Lin, W. Guan, J. Meng, W. Huang, X. Wei, Y. Zeng, J. Li, Z. Zhang, *Nano Energy* **2018**, *54*, 313–321; c) Q. Wang, C. H. Shen, S. Y. Shen, Y. F. Xu, C. G. Shi, L. Huang, J. T. Li, S. G. Sun, *ACS Appl. Mater. Interfaces* **2017**, *9*, 24731–24742; d) X. Cheng, J. Zheng, J. Lu, Y. Li, P. Yan, Y. Zhang, *Nano Energy* **2019**, *62*, 30–37; e) H. Kim, M. G. Kim, H. Y. Jeong, H. Nam, J. Cho, *Nano Lett.* **2015**, *15*, 2111–2119; f) T. Li, X.-Z. Yuan, L. Zhang, D. Song, K. Shi, C. Bock, *Electro. Energy Rev.* **2020**, *3*, 43–80.
- [5] a) P. Yang, J. Zheng, S. Kuppam, Q. Li, D. Lv, J. Xiao, G. Chen, J.-G. Zhang, C.-M. Wang, *Chem. Mater.* **2015**, *27*, 7447–7451; b) K. Xu, *Chem. Rev.* **2014**, *114*, 11503–11618; c) D. Li, H. Li, D. L. Danilov, L. Gao, X. Chen, Z. Zhang, J. Zhou, R.-A. Eichel, Y. Yang, P. H. L. Notten, *J. Power Sources* **2019**, *416*, 163–174; d) W. Zhao, J. Zheng, L. Zou, H. Jia, B. Liu, H. Wang, M. H. Engelhard, C. Wang, W. Xu, Y. Yang, J.-G. Zhang, *Adv. Energy Mater.* **2018**, *8*, 1800297.
- [6] a) S.-K. Jung, H. Gwon, J. Hong, K.-Y. Park, D.-H. Seo, H. Kim, J. Hyun, W. Yang, K. Kang, *Adv. Energy Mater.* **2014**, *4*, 1300787; b) F. Lin, I. M. Markus, D. Nordlund, T. C. Weng, M. D. Asta, H. L. Xin, M. M. Doeff, *Nat. Commun.* **2014**, *5*, 3529; c) P. Yan, J. Zheng, J. G. Zhang, C. Wang, *Nano Lett.* **2017**, *17*, 3946–3951; d) S. Hwang, S. M. Kim, S.-M. Bak, K. Y. Chung, W. Chang, *Chem. Mater.* **2015**, *27*, 6044–6052.
- [7] Y. Cho, P. Oh, J. Cho, *Nano Lett.* **2013**, *13*, 1145–1152.
- [8] M. Börner, F. Horsthemke, F. Kollmer, S. Haseloff, A. Friesen, P. Niehoff, S. Nowak, M. Winter, F. M. Schappacher, *J. Power Sources* **2016**, *335*, 45–55.
- [9] a) H. Yu, Y. Qian, M. Otani, D. Tang, S. Guo, Y. Zhu, H. Zhou, *Energy Environ. Sci.* **2014**, *7*, 1068–1078; b) J. Zheng, Y. Ye, T. Liu, Y. Xiao, C. Wang, F. Wang, F. Pan, *Acc. Chem. Res.* **2019**, *52*, 2201–2209.
- [10] a) J. Shu, R. Ma, L. Shao, M. Shui, K. Wu, M. Lao, D. Wang, N. Long, Y. Ren, *J. Power Sources* **2014**, *245*, 7–18; b) S. S. Zhang, *J. Energy Chem.* **2020**, *41*, 135–141; c) H.-H. Ryu, K.-J. Park, C. S. Yoon, Y.-K. Sun, *Chem. Mater.* **2018**, *30*, 1155–1163.
- [11] a) P. Yan, J. Zheng, T. Chen, L. Luo, Y. Jiang, K. Wang, M. Sui, J. G. Zhang, S. Zhang, C. Wang, *Nat. Commun.* **2018**, *9*, 2437; b) H. Zhang, F. Omenya, P. Yan, L. Luo, M. S. Whittingham, C. Wang, G. Zhou, *ACS Energy Lett.* **2017**, *2*, 2607–2615.
- [12] a) M. N. Obrovac, O. Mao, J. R. Dahn, *Solid State Ionics* **1998**, *112*, 9–19; b) K. Kang, G. Ceder, *Phys. Rev. B* **2006**, *74*, 094105; c) J. Lee, A. Urban, X. Li, D. Su, G. Hautier, G. Ceder, *Science* **2014**, *343*, 519–522.
- [13] a) M. Gu, I. Belharouak, J. Zheng, H. Wu, J. Xiao, A. Genc, K. Amine, S. Thevuthasan, D. R. Baer, J.-G. Zhang, N. D. Browning, J. Liu, C. Wang, *ACS Nano* **2013**, *7*, 760–767; b) H. Moriwake, A. Kuwabara, C. A. Fisher, R. Huang, T. Hitosugi, Y. H. Ikuhara, H. Oki, Y. Ikuhara, *Adv. Mater.* **2013**, *25*, 618–622; c) P. V. Ong, Z. Yang, P. V. Sushko, Y. Du, *J. Phys. Chem. Lett.* **2018**, *9*, 5515–5520; d) Q. Li, Z. Yao, E. Lee, Y. Xu, M. M. Thackeray, C. Wolverton, V. P. Dravid, J. Wu, *Nat. Commun.* **2019**, *10*, 1692.
- [14] a) Y. Gong, J. Zhang, L. Jiang, J. A. Shi, Q. Zhang, Z. Yang, D. Zou, J. Wang, X. Yu, R. Xiao, Y. S. Hu, L. Gu, H. Li, L. Chen, *J. Am. Chem. Soc.* **2017**, *139*, 4274–4277; b) Y. Gong, Y. Chen, Q. Zhang, F. Meng, J. A. Shi, X. Liu, X. Liu, J. Zhang, H. Wang, J. Wang, Q. Yu, Z. Zhang, Q. Xu, R. Xiao, Y. S. Hu, L. Gu, H. Li, X. Huang, L. Chen, *Nat. Commun.* **2018**, *9*, 3341.
- [15] J. Zheng, P. Yan, L. Estevez, C. Wang, J.-G. Zhang, *Nano Energy* **2018**, *49*, 538–548.
- [16] S. M. Bak, E. Hu, Y. Zhou, X. Yu, S. D. Senanayake, S. J. Cho, K. B. Kim, K. Y. Chung, X. Q. Yang, K. W. Nam, *ACS Appl. Mater. Interfaces* **2014**, *6*, 22594–22601.
- [17] P. Yan, J. Zheng, M. Gu, J. Xiao, J. G. Zhang, C. M. Wang, *Nat. Commun.* **2017**, *8*, 14101.
- [18] V. Pimenta, M. Sathiyaa, D. Batuk, A. M. Abakumov, D. Giaume, S. Cassaignon, D. Larcher, J.-M. Tarascon, *Chem. Mater.* **2017**, *29*, 9923–9936.
- [19] Z. Yang, P. V. Ong, Y. He, L. Wang, M. E. Bowden, W. Xu, T. C. Droubay, C. Wang, P. V. Sushko, Y. Du, *Small* **2018**, *14*, 1803108.
- [20] a) K. Märker, P. J. Reeves, C. Xu, K. J. Griffith, C. P. Grey, *Chem. Mater.* **2019**, *31*, 2545–2554; b) J. Li, L. E. Downie, L. Ma, W. Qiu, J. R. Dahn, *J. Electrochem. Soc.* **2015**, *162*, A1401–A1408.
- [21] A. Boulineau, L. Simonin, J. F. Colin, C. Bourbon, S. Patoux, *Nano Lett.* **2013**, *13*, 3857–3863.
- [22] a) Y. Makimura, S. Zheng, Y. Ikuhara, Y. Ukyo, *J. Electrochem. Soc.* **2012**, *159*, A1070–A1073; b) J. Xiao, N. A. Chernova, M. S. Whittingham, *Chem. Mater.* **2008**, *20*, 7454–7464.
- [23] R. Malik, D. Burch, M. Bazant, G. Ceder, *Nano Lett.* **2010**, *10*, 4123–4127.

Manuskript erhalten: 8. Juni 2020

Veränderte Fassung erhalten: 28. Juli 2020

Akzeptierte Fassung online: 2. August 2020

Endgültige Fassung online: 23. September 2020